

Characterization of Flow and Mixing in an SMX Static Mixer

J. M. Zalc, E. S. Szalai, and F. J. Muzzio

Dept. of Chemical and Biochemical Engineering, Rutgers University, Piscataway NJ 08855

S. Jaffer

Procter and Gamble Company, Cincinnati, OH 45202

Laminar flow and mixing of a Newtonian fluid are characterized in a four-element Koch-Glitsch SMX static mixer. The computational analysis on a fine, unstructured mesh containing more than 3.5 million tetrahedral elements led to high-resolution numerical data for velocity and pressure. Computed pressure drops agreed excellently with those in the literature. The flow in this static mixer is essentially independent of the flow rate up to $Re = 1$, thereby causing the flow characteristics to deviate substantially from those observed when $Re < 1$. Furthermore, mixing behavior is examined using Lagrangian particle tracking simulations, as well as statistical methods to facilitate comparisons with experimental data. The mixing rate calculated from the simulations agreed closely with experimentally measured values. Both exponential decrease in the variation coefficient as a function of downstream length and the evolution of a self-similar mixing structure are both evidence of chaotic mixing in the SMX mixer.

Introduction

Static mixers are widely applied and easy to use (Pahl and Muschelknautz, 1982; Sembira et al., 1988; Yoon and Choi, 1996; Heierle, 1989), but the fundamental understanding of flow and mixing in static mixers is nevertheless relatively minimal (Godfrey, 1992). In-line, continuous-flow devices are employed in a wide range of industrial processes (pharmaceutical, petrochemical, food, cosmetic, and biotechnology), and yet their design is based more on intuition, availability, and/or vendor claims than on scientific data. Efforts have been mostly aimed at creating heuristic guidelines for selecting mixing equipment based on cost, type of application, residence time, phases to be mixed, and so on (Naumann, 1982; Cybulski and Werner, 1986; Koironen et al., 1994; Joshi et al., 1995). Such an approach may help avoid gross mistakes (that nevertheless occur from time to time) such as choosing a conventional stirred tank for a powder blending operation, but it does not provide any quantitative information about flow patterns, shear rates, or mixing behavior in these devices.

The scarcity of information about flow and mixing in static mixers is partially due to their often complex construction, which makes direct, nonintrusive experimental investigations difficult. Researchers have reported pressure drop data (Boss and Czastkiewicz, 1982; Chen, 1973; Shah and Kale, 1991; Cavatorta et al., 1999), residence time distributions (Naumann, 1982; Pustelnik, 1986; Naumann, 1991; Li et al., 1998), and homogenization lengths (Alloca, 1982; Heywood et al., 1984) for a variety of static mixer geometries over the past few decades as a means of assessing flow and mixing performance. Some mixing analysis has been based on observing mixing patterns by solidifying two different color epoxies as they pass through the mixer, and make cross-sectional cuts (Middleman, 1977). This procedure is informative, especially since statistical analysis can be performed on the mixing structures observed at different axial distances, but the mixer assembly is sacrificed in the process and results are limited to the specific material used in the experiment. A recent study (Jaffer and Wood, 1998) used laser induced fluorescence to obtain information about striation widths in an assembly of clear acrylic Kenics static mixer elements. While this ap-

Correspondence concerning this article should be addressed to F. J. Muzzio.

proach is nonintrusive, experimental runs can be time-consuming and costly, especially if a number of geometric variations are considered.

With the ever-increasing speed of digital computers, the numerical investigation of flow and mixing in static mixers is becoming more common. The feasibility of using computational fluid dynamics (CFD) to study static mixers has been established by generating a flow field solution in a Kenics static mixer without any subsequent mixing analysis (Bakker and LaRoche, 1993). Laminar flow and mixing in the Kenics was computed recently (Hobbs, 1997; Avalosse and Crochet, 1997), but other static mixer geometries, including the LPD, ISG, Inliner, and SMX, have received significantly less attention in the literature (Mickaily-Huber et al., 1996; Fradette et al., 1998; Rauline et al., 1998). Although these studies all considered complex static mixer geometries, the computational grid and the velocity/pressure field solutions were based on coarse resolution. None of the previous studies consider the effects of increased flow rate and inertia. Characterizations of mixing performance were based on examining tracer mixing patterns and computing the coefficient of variance in the limit of zero Reynolds number, but none of the previous studies compared the computed mixing rates to experimentally measured ones. This article presents results for a wide range of flow rates in an SMX static mixer, which span over six orders of magnitude from 10^{-4} to 10^2 .

This article focuses on the mixing of two streams with similar physical properties and flow rates. The mixing performance is evaluated of the SMX mixer by using Lagrangian particle tracking methods to examine the evolution of mixing patterns. Analysis of mixture homogeneity based on statistical techniques yields quantitative data that are experimentally measurable. To the best of our knowledge, a direct comparison between computational and experimental mixing performance has not been published for the SMX system.

System Geometry and Computational Techniques

The computational study of a Koch-Glitsch SMX static mixer commonly used for applications involving viscous media is the focus of this work. This mixer has one of the most complex constructions among commonly employed in-line mixers. A four-element mixer is shown in Figure 1 where the cylindrical mixer housing has been removed for visual clarity. The series of criss-crossing blades, arranged axially in a pipe, repeatedly divide the passing fluid into layers and spread them over the pipe cross-section. For the case considered here, each mixer element has a diameter D_m of 0.07715 m and a length-to-diameter ratio equal to one. The thickness of each blade is 0.001928 m and the entire assembly is located inside an open tube with a diameter D_t of 0.07872 m. In practice, there is roughly a 2% difference between the mixer element diameter and tube diameter, because the mixer elements are slid into a tube of slightly larger diameter, rather than welded to the pipe. An open-tube section of one pipe diameter is added to the geometry in the simulations, so that entrance and exit effects are eliminated near the static mixer region.

Numerical solutions of velocity and pressure in three-dimensional (3-D) devices, such as the SMX static mixer, all involve these common steps: (1) generate a computational

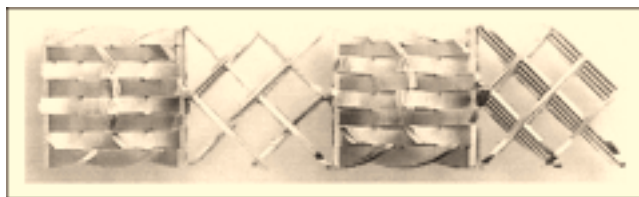


Figure 1. Four-element SMX static mixer assembly.

model of the system geometry; (2) discretize the 3-D flow domain to small control volumes; (3) solve the resulting algebraic system of equations for the velocity and pressure field in the device. In this study, the geometry of the mixer assembly was modeled by preBFC (Fluent Inc., Lebanon, NH) and an unstructured tetrahedral mesh of the fluid volume was made using TGrid (Fluent Inc., Lebanon, NH). The mesh used for all subsequent computations in this analysis contains 685,432 nodes and 3,530,488 first-order tetrahedral elements.

Once the discretization of the flow domain has been performed, software is needed to obtain approximate values for the velocity components and pressure at each of the node points. The conservation balances are represented as a matrix of algebraic equations in each small volume element, which is solved by iterative methods on a cluster of digital computers. For this purpose, we chose the CFD solver acU-Solve (ACUSIM Software, Saratoga, CA), which solves the fully-coupled mass and momentum equations based on Galerkin/least-squares finite elements with equal-order interpolation for all field variables (including pressure). In this method, a least-squares operator is added to the basic method to achieve stability of the convective terms and enforce zero divergence in velocity.

In all simulations presented, fluid properties similar to glycerine are chosen. The Newtonian fluid viscosity μ is set to a value of 0.5 kg/(m*s) and the fluid density ρ is fixed at 1,200 kg/(m³). The flow condition in static mixers is generally characterized by the open tube Reynolds number $Re = \frac{\rho \langle v_x \rangle D_t}{\mu}$ where D_t is the tube diameter and $\langle v_x \rangle$ is the mean axial velocity. For all flow conditions investigated in this work, the Re does not exceed 100 and the flow is laminar.

The inlet condition is a parabolic axial velocity profile with an average value $\langle v_x \rangle$ based on the desired Reynolds number; conditions examined here span many orders of magnitude: $Re = 10^{-4}$, 10^{-3} , 10^{-2} , 10^{-1} , 1, 10, 20, 30, 40, 50, 60, 70, 80, 90, and 100. A zero pressure condition is adopted at the outlet of the mixer since, for the incompressible flows considered here, it is only the pressure gradient that is relevant. A no-slip boundary condition is set for all wetted surfaces. The simulations were run parallel on eight HAL class 375 machines (Fujitsu, San Jose, CA) until the normalized residuals for the three velocity components and the pressure for each case converged below 10^{-4} . The calculation of the velocity and pressure fields for each Reynolds number took less than six iterations to converge, and each run was less than 1.2 h of CPU time on the cluster of eight processors.

ORCA post-processing software (Dantec, Mahwah, NJ) was used to reconstruct the computational grid and carry out sub-

sequent post-processing of the computational data. Using this software, values of field variables can be interpolated at arbitrary positions within the flow domain based on the computed values at the nodal points. An equivalent experimental investigation would be virtually impossible due to the complex geometry of the mixer elements. For instance, unless the index of refraction of the fluid and the mixer construction material were matched perfectly, optical distortion through the mixer blades would prevent the acquisition of reliable particle image velocimetry (PIV) results. The details of the interpolation scheme are similar to those previously applied to the Kenics mixer (Hobbs, 1997).

Eulerian analysis of flow in the SMX mixer

The straining motions of a fluid element are represented by the rate of deformation tensor \underline{D} , which is the symmetric part of the velocity gradient tensor $\underline{\nabla v}$, is given by

$$\underline{D} = \frac{\underline{\nabla v} + (\underline{\nabla v})^T}{2} \quad (1)$$

Here, the superscript T denotes the tensor transpose. The magnitude of the rate of deformation tensor $\xi = \sqrt{|\underline{D}:\underline{D}|} = |\sum_i \sum_j D_{ij} D_{ji}|^{1/2}$ represents the upper bound for the local rate of intermaterial area generation (Ottino, 1982). Because local values of the velocity gradient determine the local stretching, folding, and reorientation of fluid elements as they visit different locations in the flow, knowledge of the velocity gradients within the flow permits the determination of regions that have the greatest potential for mixing. Calculation of ξ is also important, because biofilm removal and cleaning often require exceeding some minimum value of ξ .

Lagrangian analysis of mixing in the SMX mixer

However, these Eulerian measures do not reveal the dynamical evolution of mixing patterns and material interfaces that are our primary concerns from a process design standpoint. In order to understand the mixing process, we simulated the evolution of mixtures by injecting massless colored tracers at the inlet of the SMX and followed their position in time (\underline{x}), by integrating along the velocity field: $d\underline{x}/dt = \underline{v}$.

Two types of injections were used in the mixing analysis:

(i) 50–50% by volume red and blue tracers, covering the entire mixer cross section uniformly. By plotting the position of tracers at various downstream distances, this type of analysis reveals the evolution of mixing patterns in a 50-50 mixture of similar fluids.

(ii) 10% by volume dark tracer particles injected at the centerline of the mixer. Building on the intensity of segregation concept (Danckwartz, 1953), the homogeneity of the system can be assessed based on statistical analysis of samples from the mixture.

One such statistical method involves computing the decrease in the variation coefficient. We adopted the following algorithm when computing the variation coefficient: a 70×70 grid of equal-size cells is placed over the mixer cross-section, and only cells that are entirely within the mixer diameter ($n_{\text{cells}} = 3,712$) are retained. Any cells falling partially or fully

outside of the circular cross section are discarded. The number-based standard deviation σ_N is given by

$$\sigma_N = \sqrt{\frac{\sum_{i=1}^{n_{\text{cells}}} (N_i - \bar{N})^2}{n_{\text{cells}} - 1}} \quad (3)$$

N_i is defined as the number of tracer particles in box i ; \bar{N} is the mean number of particles per cell. Then, the relative standard deviation (rsd) at each axial cross-section is then computed according to

$$\text{rsd} = \sqrt{\frac{(\sigma_N^2 - \sigma_\infty^2)}{\bar{N}^2}} \quad (4)$$

Here, σ_∞ is the residual value of the number-based standard deviation at the end of ten mixer elements.

Results

Average pressure drop and deformation rate

For the system examined, comparison of numerical and experimental results for pressure drop is a vital part of validation, because direct comparison of velocity vectors is very difficult due to a dearth of experimental information. Experimental measurement of planar velocity components in the SMX mixer is hindered by the complex geometry of the device.

When considering pressure drop across static mixer elements, a common approach is to define a dimensionless ratio based on the pressure drop across a static mixer divided by the pressure drop in an empty pipe of equivalent length. This ratio, called the Z factor, is essentially the increase in energy costs when static mixer elements are installed in a continuous-flow process

$$Z = \frac{\Delta P_{SM}}{\Delta P_{OT}} \quad (5)$$

Here, ΔP_{SM} is the actual pressure drop in the SMX and ΔP_{OT} is the corresponding open tube pressure drop in the same length tube (given by the Hagen-Poiseuille equation). We used a four-element SMX mixer, such as the one illustrated in Figure 1, to compute the Z factor and compare with experimentally measured values. As revealed by Figure 2, two distinct zones can be distinguished in flow behavior based on the Z factor. The Z factor is virtually independent of Re in the creeping flow regime, below $Re \leq 10$. Above $Re \geq 10$, it increases nonlinearly with increasing Re , as inertial effects become increasingly important.

Numerical values of the upstream and downstream pressure for each flow condition were computed at a reference plane 0.1cm upstream of the first mixer element and 0.1 cm downstream of the 4th mixer element, respectively. For each flow condition, the average pressure was computed at 10,000 uniformly distributed points in the mixer cross-section at each reference plane. The pressure drop, simply defined as the difference between the average values at these two axial positions, was divided by ΔP_{OT} to obtain the Z factor.

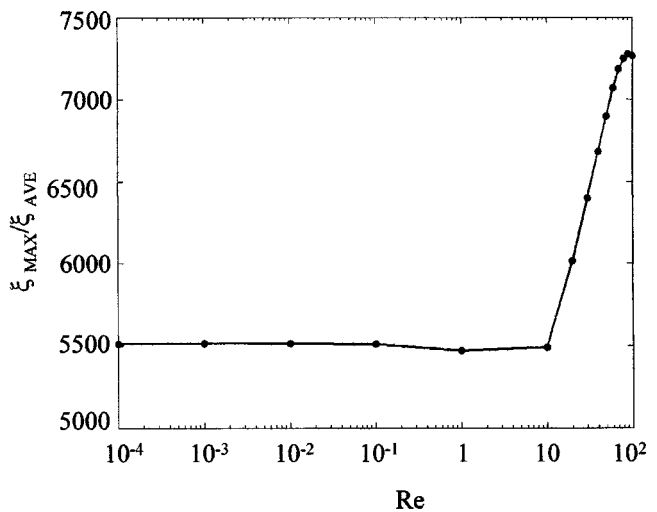
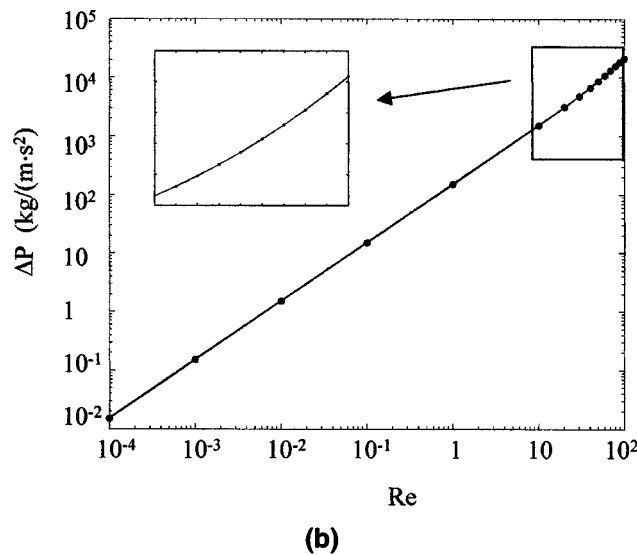
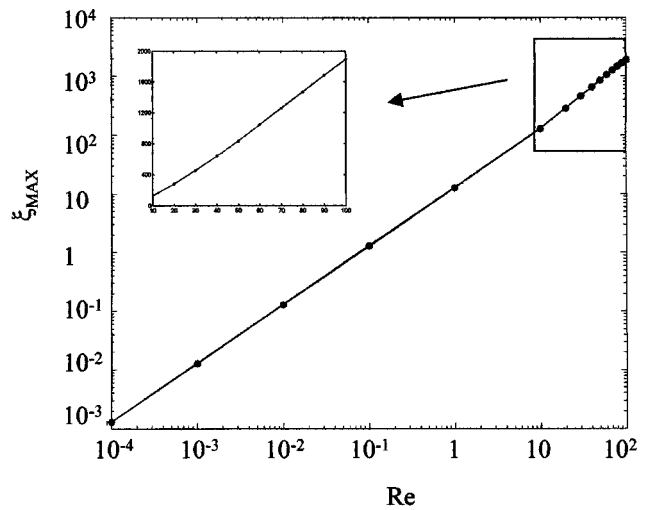
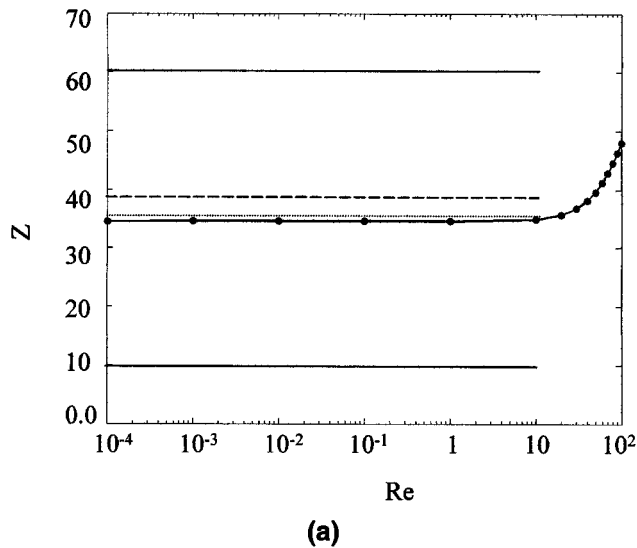


Figure 2. (a) Z factor vs. Re for computations (●—●), experimental values of Pahl and Muschelknautz (—), Alloca (---), and data from Koch-Glitsch (· · · ·); (b) computational results for pressure drop vs. $Re = 10^{-4}, 10^{-3}, 10^{-2}, 10^{-1}, 1, 10, 20, 30, 40, 50, 60, 70, 80, 90,$ and 100 .

Figure 3. (a) Maximum value of deformation tensor ξ_{\max} vs. Re ; (b) ratio of the maximum to the volume-weighted average of deformation tensor, $\xi_{\max}/\xi_{\text{ave}}$ vs. Re .

In Figure 2a, simulation results for the Z factor are compared with several sets of experimental data. The calculated Z factor is constant (34.6) for all Reynolds numbers up through 1 and increases beyond $Re = 10$, reaching a value of 48.0 for $Re = 100$. Most experimental correlations for the Z factor available in the literature apply only to cases in which $Re \leq 10$. Pahl and Muschelknautz (1982) report that Z factors for the SMX mixer can range from 10 to 60, whereas Alloca (1982) reports that the pressure drop ratio is 38.7 for slow flows. Further, Koch-Glitsch data indicate that $Z = 35$ for $Re < 10$, and our numerical results deviate by only 1.4% from these data.

With increasing inertia, the linear relationship between the flow rate and the average pressure drop vanishes. This behavior is highlighted in Figure 2b, where the average pressure drop is plotted as a function of the Reynolds number. Here, the average pressure drop is linearly proportional to the Reynolds number below $Re < 10$, but this relationship becomes nonlinear once Re exceeds 10. A very similar trend in the overall maximum and average values of deformation rate is noted as a function of the Reynolds number. For the sake of brevity, only the results for the maximum rate of deformation are shown in Figure 3a. Here, ξ_{MAX} is the maximum deformation over all 3,530,488 tetrahedra as a function of the Reynolds number. It increases at a constant rate with Re under $Re \leq 10$, and becomes a nonlinear function of flow rate as Re exceeds 10. The results for ξ_{AVE} vs. Re are quite similar, except the scale on the vertical axis is much lower in that case.

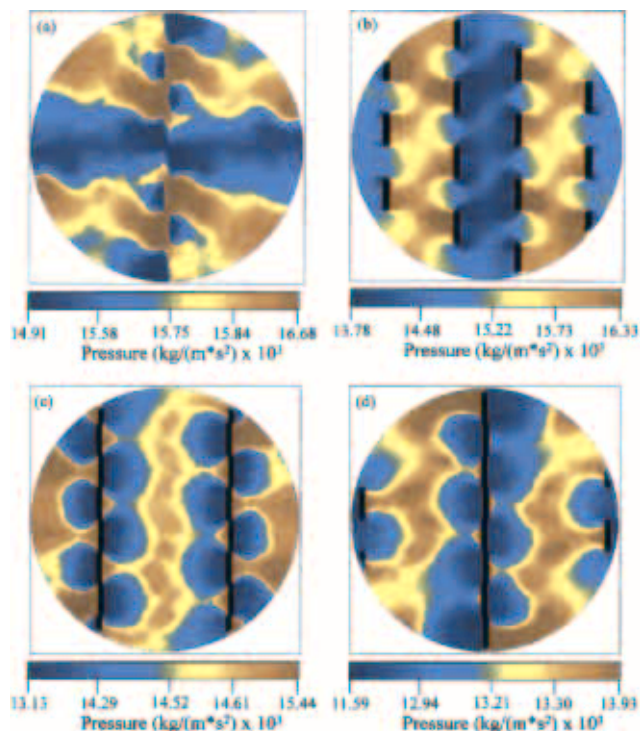


Figure 4. Contour of pressure for $Re = 100$ at four axial distances.

(a) $X = 1L$; (b) at $(1 + 1/8)L$; (c) at $(1 + 2/8)L$; (d) at $(1 + 4/8)L$.

Interesting behavior is revealed that is not evident from plotting ξ_{MAX} or ξ_{AVE} individually, but rather define a ratio of the maximum to the average value of ξ . This ratio, ξ_{MAX}/ξ_{AVE} is examined in Figure 3b as a function of the Reynolds number, indicating that it remains virtually constant at about 5,500 until $Re = 10$, beyond which it rises sharply with increasing Re .

Spatial distributions of pressure, and deformation rate

The spatial distributions of pressure, axial velocity, transverse velocity, and ξ were computed for 60,000 uniformly distributed points covering the cross-section of the SMX mixer for numerous axial distances. For visual display, the points along each plane were sorted in increasing order of magnitude and plotted in dark blue, followed by light blue, green, yellow, orange, and red. The color ranges were chosen so approximately an equal number of points are represented by each color for the pressure field and the magnitude of deformation.

Figures 4a–4d illustrate how the pressure field varies in the second element at $Re = 100$. The four plots in Figures 4a–4d correspond to axial distances of $X = 1L$, $(1 + 1/8)L$, $(1 + 2/8)L$ and $(1 + 4/8)L$, respectively, where L is the length of one SMX mixer element. Even though the spatial distributions of pressure at lower Reynolds numbers vary slightly, they share many important characteristics. For each flow rate examined, the pressure field looks highly nonuniform in each cross-section, but exhibits symmetry about the center of the plane and the mean pressure decreases with increasing axial

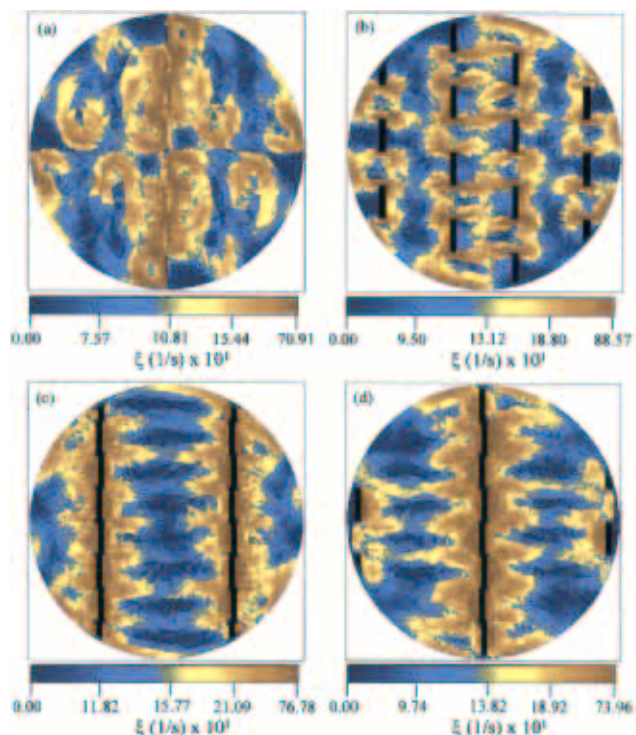


Figure 5. Contour of ξ for $Re = 100$ at axial distances.

(a) at $X = 1L$; (b) at $(1 + 1/8)L$; (c) at $(1 + 2/8)L$; (d) at $(1 + 4/8)L$.

distance through the mixer. The maximum pressure variation for the four plots in Figure 4 is 20.1%, and when all 17 planes in the second and third mixer elements are considered, the maximum pressure variation in a cross-section is 62.7% for $Re = 100$. Such large variations are due to the complex mixer geometry and cause strong transverse flows. An implication of the uneven distribution of pressure is that cavitation is likely to occur in the low-pressure regions. Knowing the symmetry and spatial patterns in the pressure field could be exploited in applications requiring controlled cavitation.

Figures 5a–5d show contour plots of ξ for $Re = 100$ for the same cross-sections as in Figures 4a–4d. It is apparent that the distributions of ξ are also nonuniform in each cross-section, similar to the pressure field. In all cases, the regions of highest ξ exist near the blades of the mixer. Of the four cross-sections shown, the highest values of ξ are observed at $X = (1 + 1/8)L$. Since ξ is the upper bound of the deformation rate, this is an indication that significant variations in local mixing rates could also occur in the flow.

Velocity field as a function of flow rate

The flow fields at $Re = 10$ and $Re = 100$ are likely to be very different, as inertia plays an increasingly important role above $Re = 10$.

The axial component of the flow at $Re = 100$ is illustrated in Figures 6a–6d, where symmetry about the axis of the mixer is immediately evident. This finding is not surprising, considering that similar symmetry exists in the pressure field. Visual display of the results is based on a slightly different method for the velocity contour plots, than the one discussed

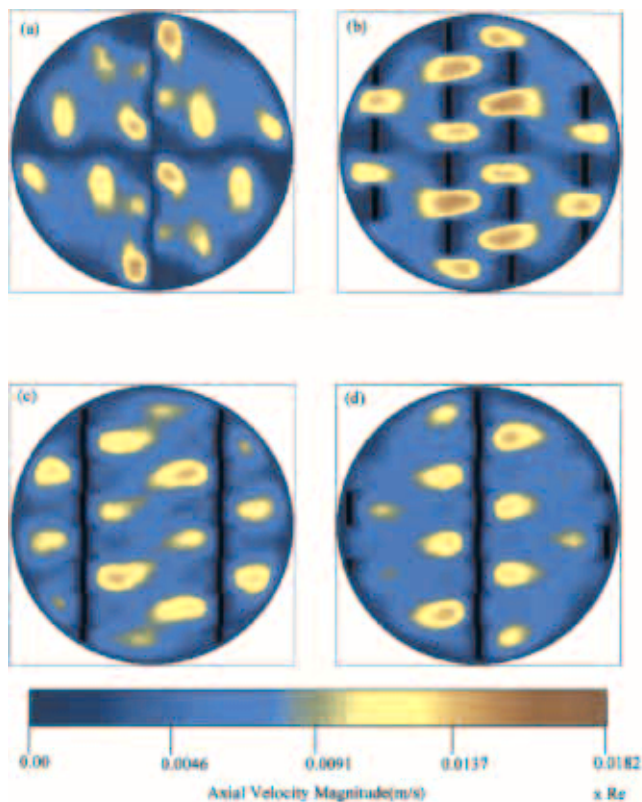


Figure 6. Contour of v_x (axial velocity) for $Re = 100$ at axial distances.

(a) at $X = 1L$; (b) at $(1 + 1/8)L$; (c) at $(1 + 2/8)L$; (d) at $(1 + 4/8)L$.

earlier for ΔP and ξ . The velocity components for each contour plot were grouped into equal-size bins and color-coded based on equal incremental values. Four contour plots of the axial velocity are given in Figures 6a–6d for $Re = 100$, corresponding to the same downstream distances that were discussed earlier for ΔP and ξ . The highest axial velocities occur in the channels aligned with the rows of mixer blades. This is true, in general, about the flow at other flow rates as well. Comparing the axial velocity contours (Figures 6a–6d) with those of the planar component at corresponding distances (Figures 7a–7d), it is immediately apparent that the magnitudes of the transverse velocities are of the same order of magnitude as the axial velocities. Directions of the planar velocity components show flow around the mixer blades in each cross section, as streams of fluid separate and reunite after passing each mixer blade. For $Re = 100$, higher transverse velocities exist at $X = (1 + 4/8)L$, than at the other three planes shown in Figure 7. At a lower flow rate, as in the case of $Re = 10$, higher transverse velocities are observed at $X = (1 + 1/8)L$ (figure not shown). As a result of inertial effects, the region of highest transverse velocity shifts further downstream in each element as the Reynolds number is increased.

Statistical analysis of velocity components

So far, the illustration of the flow and pressure fields in the SMX static mixer has been mainly qualitative. A statistical

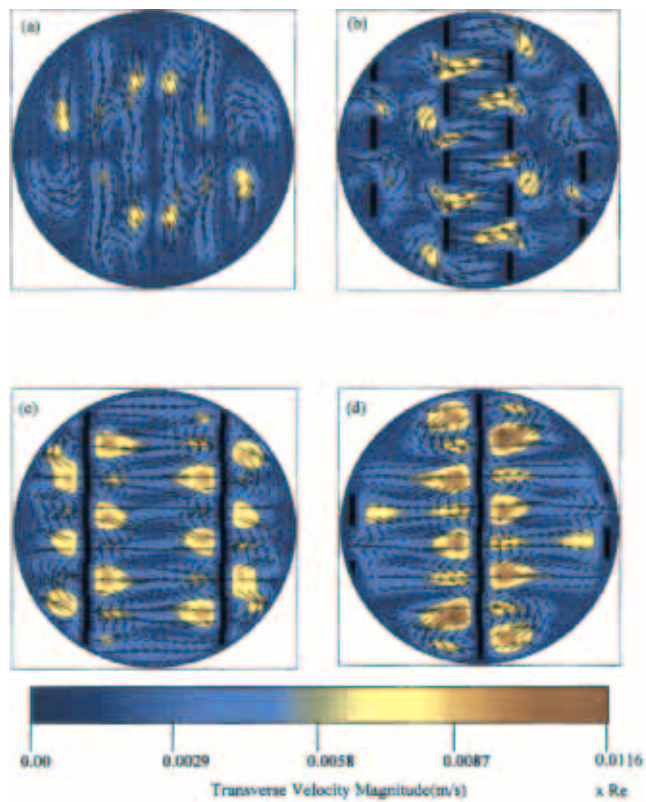


Figure 7. Contour of v_t (transverse velocity) for $Re = 100$ at axial distances.

(a) at $X = 1L$; (b) at $(1 + 1/8)L$; (c) at $(1 + 2/8)L$; (d) at $(1 + 4/8)L$.

analysis of the velocity components is undertaken next, because even small differences in the flow field at different Reynolds numbers can translate into significant differences in mixing performance.

The axial, radial, and azimuthal components of velocity are normalized with respect to their mean magnitudes

$$v_x^* = \frac{v_x}{\langle |v_x| \rangle}, v_r^* = \frac{v_r}{\langle |v_r| \rangle} \quad \text{and} \quad v_\theta^* = \frac{v_\theta}{\langle |v_\theta| \rangle} \quad (6)$$

The probability distribution functions (PDFs) for the velocity components are then constructed according to

$$F(v_a^*) = \frac{1}{N} \frac{dN(v_a^*)}{dv_a^*} \quad \text{where} \quad a = x, r, \text{ or } \theta \quad (7)$$

Here, $N = 60,000$ is the total number of velocity vectors in a given plane and $dN(v_a^*)$ is the fraction that have values between v_a^* and $v_a^* + dv_a^*$. The axial velocity distributions for $Re = 0.1$ and $Re = 1$ are very similar to each other, but at higher Reynolds numbers progressively greater deviations are observed. Consider the distribution of normalized axial velocities for all the Reynolds numbers ($Re = 0.1, 1, 10, \text{ and } 100$) halfway into the second mixer element. Figure 8a reveals the distribution of v_x^* at an axial distance $X = (1 + 4/8)L$, where L represents the length of one SMX element. Flows in the

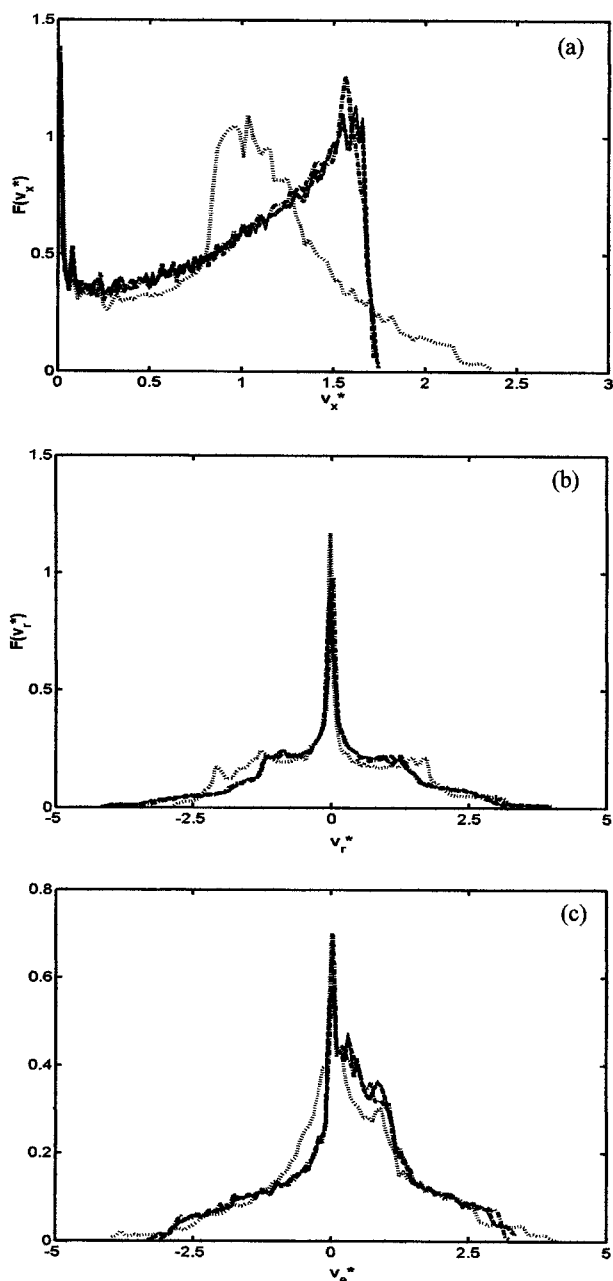


Figure 8. PDFs of normalized axial (a), radial (b) and (c) azimuthal velocity components at $(1 + 4/8)L$ for four flow rates.

$Re = 0.1$ (—), $Re = 1$ (---), $Re = 10$ (-·-), and 100 (·····).

creeping flow regime ($Re = 0.1$, $Re = 1$, and $Re = 10$) have distributions that drop sharply at $v_x^* \approx 1.8$ in the first cross-section and at $v_x^* \approx 1.7$ for the second plane. On the other hand, the PDFs at $Re = 100$ decrease gradually and extend toward $v_x^* = 2.5$, while possessing large peaks at $v_x^* \approx 0.8$. We expect that significant differences exist in residence time distributions at each flow rate in accordance with the axial velocity distributions.

The differences in flow characteristics at different Reynolds numbers are less evident in the distributions of the normal-

ized radial or azimuthal velocity components. The PDFs for the radial component, shown at the midpoint of the second mixer element in Figure 8b, possess a large peak at $v_r^* = 0$ and are almost perfectly symmetric about this peak. Distributions of the azimuthal component at the same axial distance, as illustrated in Figure 8c, range from -4.5 to 4.5 , but not as symmetric around their mode at 0 as the values of v_r^* .

Evolution of mixing structures in the SMX mixer

We now consider the mixing characteristics of the SMX. We first investigate the mixing of two fluid streams (one dyed red and the other blue) with equal flow and similar physical properties. The two streams are represented in the computations as massless point tracers, all placed 1 cm upstream of the first mixer element. A total of 201,881 passive tracers are distributed uniformly at the inlet. Particles initially located in the upper half of the cross-section are colored red and those in the lower half are blue.

The evolution of the mixing structure for $Re = 1$ is shown in Figures 9a–9f, where pictures correspond to cross-sections at the end of 0.25, 0.5, 0.75, 1.0, 1.5, and 2.0 mixer elements in Figures 9a–9f, respectively. After passing through a quar-

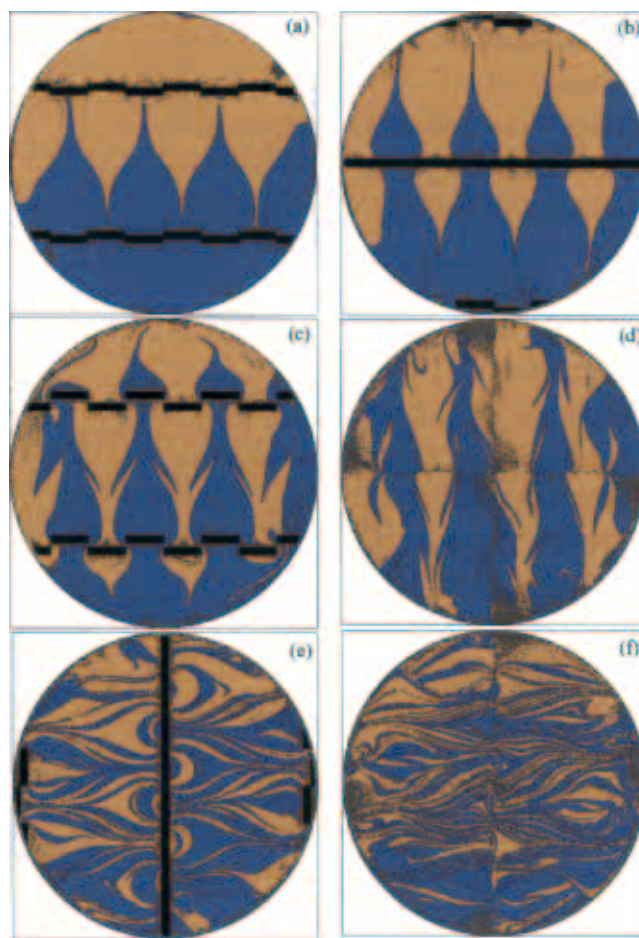


Figure 9. Computed mixing patterns for a 50-50 injection for $Re = 1$ at the end of (a) 0.25, (b) 0.50, (c) 0.75, (d) 1.0, (e) 1.5 and (f) 2.0 mixer elements.

ter of an element, the interface between the two fluid streams is stretched into a “spade-like” structure, extending toward the top and bottom part of the tube wall (a). Halfway through the SMX element the structure extends further, until it is cut again by a new series of mixer blades (b). Each time a portion of fluid is split by a mixer blade downstream, a new spike appears in the evolving mixing structure as seen after 0.75 (a) and 1 element (d). By the end of 1.5 mixer elements (e), the mixing structure evolves into a layered structure similar to the one in (b), but new folds are showing with local orientations identical to those in (b). This feature indicates self-similarity of the mixing structures created in the SMX static mixer, suggesting that as it was also the case in other industrially relevant systems; mixing in this device is driven by a spatially-periodic chaotic flow.

Quantitative evaluation of mixing performance

We extend the mixing analysis by computing the relative standard deviation (rsd) in the SMX. Equations 4 and 5 and the algorithm described in that section are employed to compute the relative standard deviation at $Re = 1$. This value of the Reynolds number is chosen because experimental measurements of rsd in an equivalent SMX geometry have been reported at this condition (Streiff, 1979). We examined the spreading of an injection of 10% by volume tracer fluid, and computed the fractional amount of tracer in different areas of the mixer. The computed relative standard deviation at each cross-section was scaled by a constant. The scaling constant is the coefficient of variance, which is 3.0 for a 10% injection ($\bar{C} = 0.1$) for a completely segregated initial condition. Scaling the rsd data in this fashion means shifting the data vertically to facilitate comparison with experimental

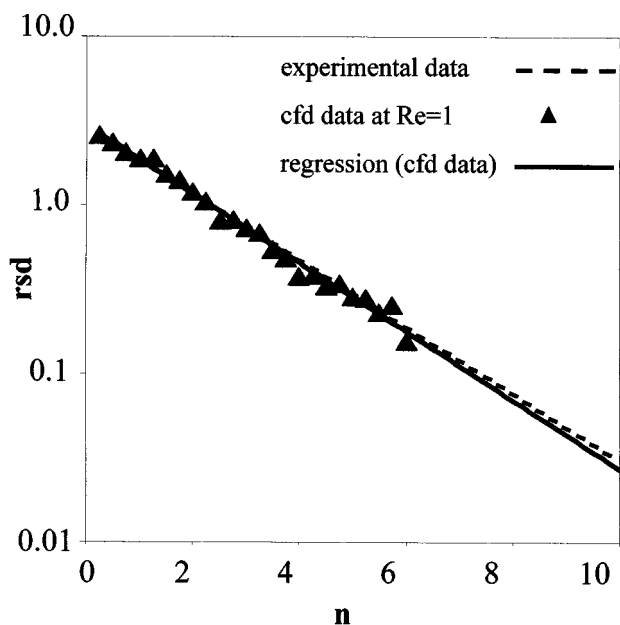


Figure 10. Computed and experimental relative standard deviation in the SMX mixer vs. number of mixer elements for $Re = 1$.

Experimental data from Streiff.

data, but does not affect the slope of each curve, which represents the mixing rate.

Figure 10 shows the decrease in rsd with the number of mixer elements for fluid injected at the mixer centerline at $Re = 1$. An exponential reduction in the rsd is maintained over six mixer elements. Linear regression of the simulation data is performed to compute the mixing rate, which is equivalent to the slope on a log scale. The correlation coefficient of 0.989 for the data set indicates a very good fit on a logarithmic scale. The computed mixing rate (the slope from the regression analysis) is 0.4703 per element. The agreement is excellent between our numerical results and the experimental data reported by Streiff, and it is maintained over the full length of 10 SMX elements considered.

Effects of flow rate on mixing performance

In order to examine the effects of increasing inertia on flow and mixing in the SMX, mixing patterns at two other flow rates ($Re = 30$ and $Re = 100$) were computed. Note that mixing performance is independent of Re when $Re < 1$ for Newtonian fluids. Figures 11a–11f show the mixing patterns at $Re = 30$ for cross-sections after 0.25, 0.5, 0.75, 1.0, 1.5, and

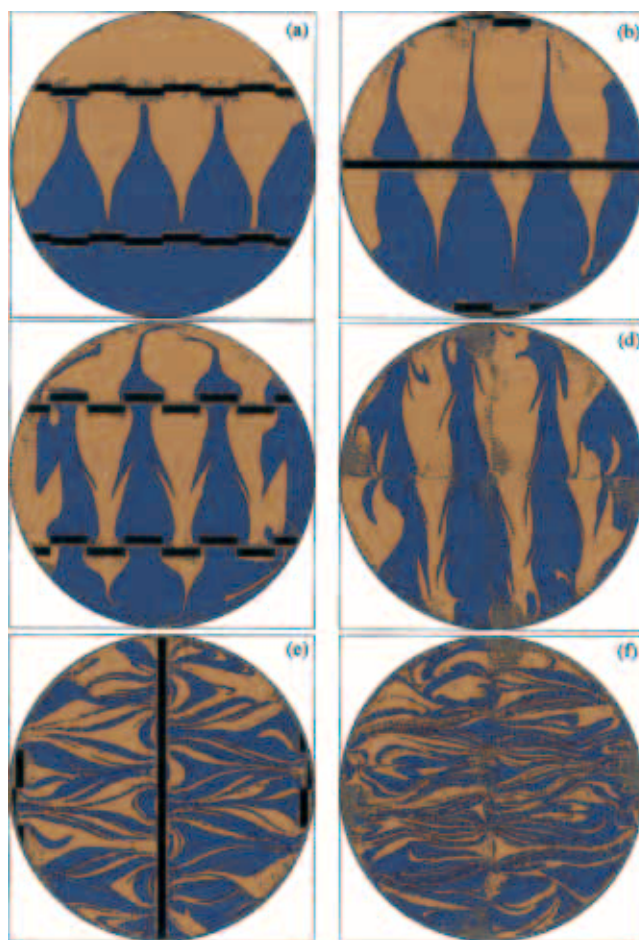


Figure 11. Computed mixing patterns for a 50-50 injection for $Re = 30$ at the end of (a) 0.25, (b) 0.50, (c) 0.75, (d) 1.0, (e) 1.5 and (f) 2.0 mixer elements.

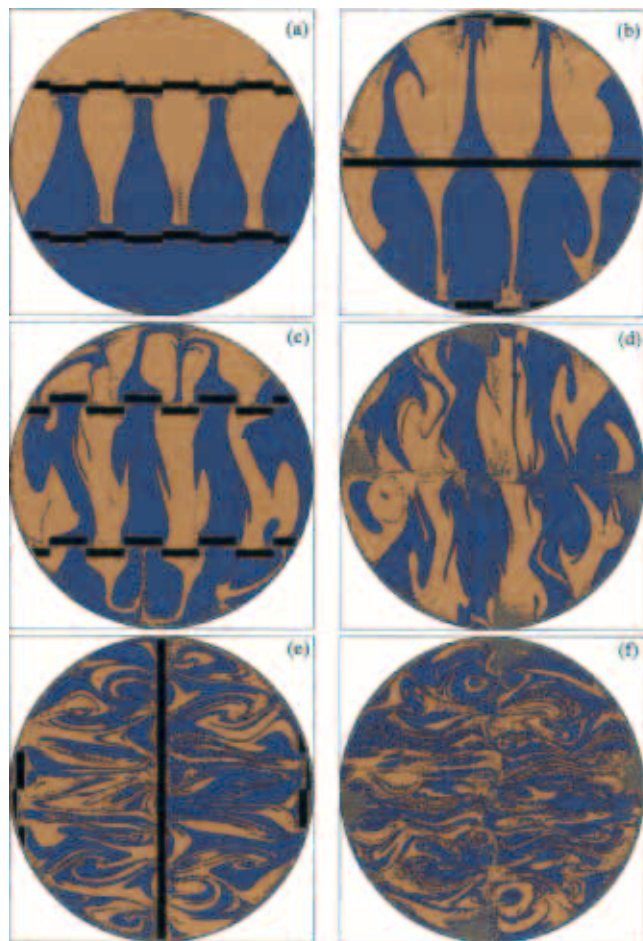


Figure 12. Computed mixing patterns for a 50-50 injection for $Re = 100$ at the end of (a) 0.25, (b) 0.50, (c) 0.75, (d) 1.0, (e) 1.5 and (f) 2.0 mixer elements.

2.0 mixer elements, respectively. These represent the same axial distances as in Figures 9a–9f, where $Re = 1$ was considered. Only minor differences in the mixing patterns exist between the $Re = 30$ flow and the $Re = 1$ case, suggesting that flow rates up to $Re = 30$ do not have a significant effect on the performance of the SMX mixer. Figures 12a–12f reveal mixing patterns generated by the $Re = 100$ flow at the same downstream axial cross-sections. These results are significantly different from the previous two flows. The symmetry in the spike-like structures that exist at lower flow rates is broken up by inertial effects even after 1/2 mixer element (Figure 12b). Larger striations of dark dye invade the other fluid stream at this higher flow rate as the blades cut and fold the fluid filaments. By the time the fluid passed through all four SMX elements (Figure 12f), it appears as homogeneous as the other two flow rate cases.

The relative standard deviation (rsd) was computed for the $Re = 30$ and $Re = 100$ case to facilitate quantitative comparison with the lowest flow rate ($Re = 1$) discussed earlier. Figure 13 shows the rsd values computed at each flow rate as a function of axial distance in terms of mixer elements. The simulation data for the lowest Re case, which was compared

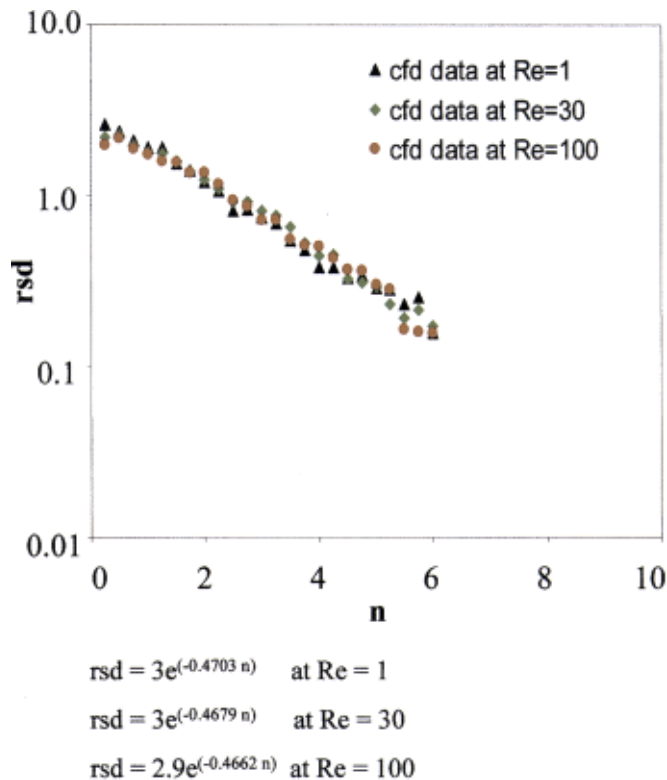


Figure 13. Computed relative standard deviation in the SMX mixer vs. number of mixer elements for three flow rates.

$Re = 1$, $Re = 30$, and $Re = 100$.

with experiments in Figure 10, is repeated here for the sake of comparison, and the rsd from the simulations of the other two flow rates is also plotted. The decrease in the relative standard deviation can be used to compare the relative mixing rate for each flow rate considered. The decrease in the relative standard deviation can be used to compare the relative mixing rate for each flow rate considered. The computational data for each Re number was fitted to a function of the form $rsd = \alpha e^{(-\beta n)}$, where n represents the number of SMX mixing elements. Table 1 summarizes the computed mixing rates (β for each flow rate):

A trend of decreasing rates with increasing Re is apparent, which is an indication of better mixing performance per element at lower flow rates. According to Table 1, the rate of decrease in rsd is greatest for the $Re = 100$ flow. Bearing residence time constraints, using lower flow rates in the SMX is further warranted by considering that the energy for flow in static mixers is directly proportional to the system pressure drop. In other words, the higher flow rate required, the greater the energy cost is to achieve equivalent mixing per

Table 1. Computed Mixing Rates as a Function of Reynolds Number

Re	β
1	0.4703
30	0.4679
100	0.4662

element. Flows above $Re = 10$ produce slightly less effective mixing at a greater energy cost. Taking both the mixing rates and energy requirements into account as a function of increasing Re numbers, it is recommended that the lowest practical flow rates are used in the SMX mixer in applications.

Conclusions

The objective of this article was to assess flow and mixing characteristics of the SMX mixer at low and moderate Reynolds numbers. For that purpose, numerical simulations were conducted using a very fine (> 3.5 million tetrahedra) unstructured mesh and each simulation converged within 1.2 h of CPU time. Results for laminar flow were presented for a wide range of flow conditions, where the Reynolds number was varied over seven orders of magnitude. The computational results for the pressure drop factor Z agree very well ($< 1.5\%$ difference) with experimental data from the manufacturer and with literature values.

The effect of Reynolds number on flow in the SMX static mixer was analyzed by both qualitative and quantitative methods by comparing color contour plots and probability distribution functions of the velocity components, and examining the pressure field and the magnitude of the deformation tensor. It was found that the flow is essentially independent of Re for $Re \leq 1$, while substantial deviations occur at increasingly higher Reynolds numbers where inertial forces are significant.

The distributive mixing performance of the SMX was described for two fluid streams with equal volume, and the emerging pattern of material striations revealed a self-similar evolution of mixing topology. The mixing rate, based on the relative standard deviation, was computed and compared with experimental data in a six-element SMX. Excellent agreement is obtained between the computational and experimental data set for a 10% centerline injection. The exponential decrease of the relative standard deviation at three different flow rates is further evidence for the existence of chaotic flow and mixing in this static mixer. We observed a trend of decreasing rates of relative standard deviation with increasing flow rate in the SMX, suggesting that lower flow rates produce more effective mixing at a smaller energy cost. Thus, it is recommended to use the lowest practical flow rates in viscous mixing applications.

Literature Cited

- Alloca, P. T., "Mixing Efficiency of Static Mixing Units in Laminar Flow," *Fiber Producer*, 12 (1982).
- Avalosse, Th., and M. J. Crochet, "Finite-Element Simulation of Mixing: 2. Three-Dimensional Flow through a Kenics Mixer," *AIChE J.*, **43**, 3 (1997).
- Bakker, A., and R. LaRoche, "Flow and Mixing with Kenics Static Mixers," *Cray Channels*, **15**, 25 (1993).
- Boss, J., and W. Czastkiewicz, "Principles of Scale-Up for Laminar Mixing Processes of Newtonian Fluids in Static Mixers," *Int. Chem. Eng.*, **22**, 362 (1982).
- Cavatorta, O. N., and U. Bohm, "Fluid Dynamic and Mass Transfer Behavior of Static Mixers and Regular Packings," *AIChE J.*, **45**, 938 (1999).
- Chen, S. J., "In-Line Continuous Mixing and Processing of Cosmetic Products," *J. Soc. Cosmet. Chem.*, **24**, 639 (1973).
- Cybulski, A., and K. Werner, "Static Mixers -- Criteria for Applications and Selection," *Int. Chem. Eng.*, **26**, 171 (1986).
- Danckwartz, P. V., "Continuous Flow Systems, Distribution of Residence Times," *Chem. Eng. Sci.*, **2**, 1 (1953).
- Fradette, L., H. Z. Li, and L. Choplin, "3D Finite Element Simulation of Fluid Flow through a SMX Static Mixer," *Comput. Chem. Eng.*, **22S**, 759 (1998).
- Godfrey, J. C., "Static Mixers," *Mixing in the Process Industries*, N. Harnby, M. F. Edwards, and A.W. Nienow, eds. (1992).
- Heierle, A., "Static Mixer-Heat Exchangers," *Chem. Plant & Processing* (1989).
- Heywood, N. I., L. J. Viney, and I. W. Stewart, "Mixing Efficiencies and Energy Requirements of Various Motionless Mixer Designs for Laminar Mixing Applications," *Institution of Chem. Engineers Symp. Ser.*, **89**, 147 (1984).
- Hobbs, D. M., "Characterization of a Kenics Static Mixer under Laminar Flow Conditions," *PhD Thesis*, Rutgers Univ. (1997).
- Jaffer, S. A., and P. E. Wood, "Quantification of Laminar Mixing in the Kenics Static Mixer: An Experimental Study," *Can. J. Chem. Eng.*, **76**, 516 (1998).
- Joshi, P., K. D. P. Nigam, and E. B. Naumann, "The Kenics Static Mixer: New Data and Proposed Correlations," *Chem. Eng. J.*, **59**, 265 (1995).
- Koironen, T., A. Kraslawski, and L. Nyström, "Knowledge-Based System for Mixing Type Selection," *Ind. Eng. Chem. Res.*, **33**, 1756 (1994).
- Li, H. Z., C. Fasol, and L. Choplin, "Residence Time Distribution of Rheologically Complex Fluids Passing through a Sulzer SMX Static Mixer," *Chem. Eng. Comm.*, **165**, 1 (1998).
- Mickaily-Huber, E. S., F. Bertrand, P. Tanguy, T. Meyer, A. Renken, F. S. Rys, and M. Wehrli, "Numerical Simulations of Mixing in an SMRX Static Mixer," *Chem. Eng. J.*, **63**, 117 (1996).
- Middleman, S., *Fundamentals of Polymer Processing*, McGraw-Hill, New York (1977).
- Naumann, E. B., "Reactions and Residence Time Distributions in Motionless Mixers," *Can. J. Chem. Eng.*, **60**, 136 (1982).
- Naumann, E. B., "On Residence Time and Trajectory Calculation in Motionless Mixers," *Chem. Eng. J.*, **47**, 141 (1991).
- Nigam, K. D. P., and E. B. Naumann, "Residence Time Distributions of Power Law Fluids in Motionless Mixers," *Can. J. Chem. Eng.*, **63**, 519 (1985).
- Ottino, J. M., "Description of Mixing with Diffusion and Reaction in Terms of the Concept of Material Surfaces," *J. Fluid Mech.*, **114**, 83 (1982).
- Pahl, M. H., and E. Muschelknautz, "Static Mixers and their Applications," *Int. Chem. Eng.*, **22**, 197 (1982).
- Pustelnik, P., "Investigation of Residence Time Distribution in Kenics Static Mixers," *Chem. Eng. Prog.*, **102**, 147 (1986).
- Rauline, D., P. Tanguy, J. LeBlévec, and J. Bousquet, "Numerical Investigation of the Performance of Several Static Mixers," *Can. J. Chem. Eng.*, **76**, 527 (1998).
- Sembira, A. N., J. C. Merchuk, and D. Wolf, "Characteristics of a Motionless Mixer for Dispersion of Immiscible Fluids: III. Dynamic Behavior of the Average Drop Size and Dispersed Phase Hold-Up," *Chem. Eng. Sci.*, **43**, 373 (1988).
- Streff, F. A., "Adapted Motionless Mixer Design," *Third European Conf. on Mixing*, Paper C2, 171 (1979).
- Shah, N. F., and D. D. Kale, "Pressure Drop for Laminar Flow of Non-Newtonian Fluids in Static Mixers," *Chem. Eng. Sci.*, **46**, 2159 (1991).
- Wang, K. B., and L. T. Fan, "Mass Transfer in Bubble Columns Packed with Motionless Mixers," *Chem. Eng. Sci.*, **33**, 945 (1978).
- Yoon, W. J., and K. Y. Choi, "Polymerization of Styrene in a Continuous Filled Tubular Reactor," *Poly. Sci. Eng.*, **36**, 65 (1996).

Manuscript received Oct. 22, 1999, and revision received Sept. 12, 2001.